ADVANCED MATERIALS
www.advmat.de

Terahertz In-Sensor Computing Utilizing Photothermoelectric Thin Films

He Shao, Yuxuan Zhang, Zhengxun Lai, Jiachi Liao, Bowen Li, Weijun Wang, Pengshan Xie, Baojie Chen, Chi Hou Chan, You Meng,* and Johnny C. Ho**

Terahertz (THz) detection is pivotal for biomedical diagnostics and security screening, enabled by its non-ionizing nature and characteristic "fingerprint" spectra. However, weak THz–matter interactions, energy-intensive processing, and complex hardware integration hinder its practical use. To this aim, a layered bismuth selenide (Bi_2Se_3)-based THz detection array is fabricated via low-temperature pulse irradiation synthesis (PIS), exhibiting a tunable thermally coupled bidirectional response. The intrinsic photothermoelectric (PTE) effect enables adaptive in-sensor THz signal processing, achieving 200 V W^{-1} responsivity and <5 ms response time at 0.3 THz in a self-powered mode. Integrated in-sensor computing enhances accuracy through real-time noise suppression, edge detection, and feature extraction. The array also demonstrates high imaging performance, with a >90% recall rate for concealed object detection. This work provides a scalable, high-precision THz sensing platform with transformative potential for biomedical and security applications.

1. Introduction

Terahertz (THz) detection has gained significant attention in biomedical diagnostics, security screening, and non-destructive testing, enabled by its ability to penetrate non-metallic materials while remaining non-ionizing.[1–3] However, the widespread utilization of THz detection is hindered by the weak THz–matter interaction, the low absorption efficiency of conventional semiconductor materials, and the dependence on bulky, power-intensive external processing units.[4,5] Recent advances in THz detection technologies have focused primarily on improving the sensitivity and detection efficiency of THz-sensitive materials. For instance, the exploration of new materials, such as topological semimetals and quantum materials, has improved the efficiency and functionality of THz devices.[6–10] However, much less attention has been paid to integrating computational capabilities within the THz detection hardware. Specifically, current THz detection systems require substantial software and hardware resources to process signals, extract features, and enhance detection performance.[11,12] Therefore, developing THz detectors with fused processing functionalities is crucial for advancing THz detection technology.

The emerging in-sensor computing architecture integrates computational functionalities directly into the sensors. It enables real-time signal processing, such as noise filtering, contrast enhancement, and feature extraction, without external computing resources.[13] This capability is particularly crucial in the THz domain, where signals are inherently weak and susceptible to noise, making real-time THz signal extraction and analysis challenging. In this regard, in-sensor computing would solve these challenges by embedding essential processing functions at the detection point, allowing for real-time and more accurate results.[14] This approach would not only enhance the efficiency of THz detection but also open the door for developing

H. Shao, Y. Zhang, J. Liao, B. Li, W. Wang, P. Xie, J. C. Ho
Department of Materials Science and Engineering
City University of Hong Kong
Hong Kong 999077, China
E-mail: johnnyho@cityu.edu.hk

Z. Lai, Y. Meng
National Key Laboratory of Power Semiconductor and Integration Technology
Engineering Research Center of Advanced Semiconductor Technology and Application of Ministry of Education
College of Semiconductors (College of Integrated Circuits)
Hunan University
Changsha 410082, China
E-mail: youmeng@hnu.edu.cn

The ORCID identification number(s) for the author(s) of this article can be found under https://doi.org/10.1002/adma.202505719

DOI: 10.1002/adma.202505719

B. Chen, C. H. Chan
State Key Laboratory of Terahertz and Millimeter Waves
City University of Hong Kong
Hong Kong 999077, China
E-mail: eechic@cityu.edu.hk

C. H. Chan
Department of Electrical Engineering
City University of Hong Kong
Hong Kong 999077, China

J. C. Ho
Shenzhen Research Institute
City University of Hong Kong
Shenzhen 518057, China

J. C. Ho
Institute for Materials Chemistry and Engineering
Kyushu University
Fukuoka 816 8580, Japan

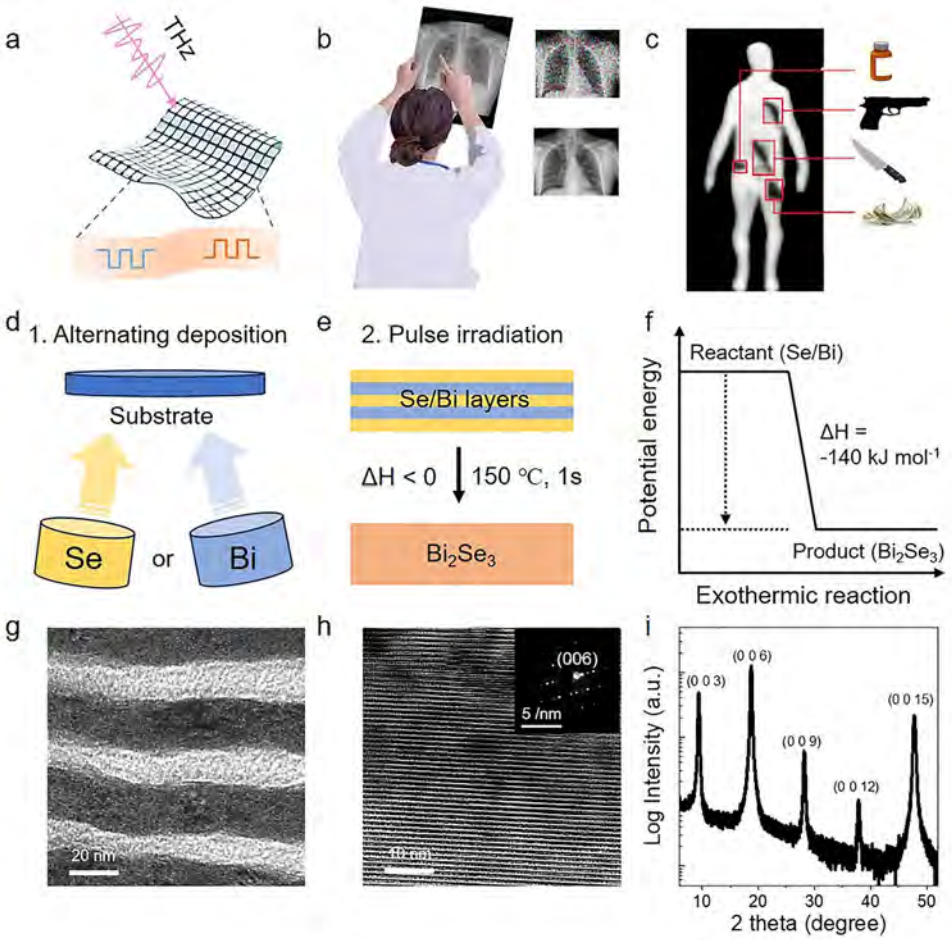

Figure 1. a) Schematic illustration of the THz photothermoelectric (PTE) sensor array for THz detection. b) Conceptual representation of THz sensing applications in medical diagnostics. c) Illustration of THz-based security screening for detecting concealed objects. d,e) Fabrication schematic of Bi_2Se_3 thin films before and after the PIS process. f) Schematic diagram of the negative formation enthalpy of the PIS process. HRTEM images of samples g) before and h) after the PIS process. i) XRD pattern of oriented Bi_2Se_3 thin films.

intelligent, adaptive THz detection systems. Overall, incorporating in-sensor computing holds promise in addressing the limitations of traditional THz detection systems, which is a crucial yet underexplored area to date.

To this aim, this work presents a layered bismuth selenide (Bi_2Se_3) -based THz detection array, fabricated via a low-temperature pulse irradiation synthesis (PIS), that exhibits a tunable thermal-coupled bi-directional response (**Figure 1a**). The intrinsic photothermoelectric (PTE) characteristic allows for dynamic modulation of the photovoltage, facilitating adaptive in-sensor THz signal processing. Operating with a self-powered mode, a responsivity of 200 V W^{-1} and a response time of less than 5 ms were achieved at 0.3 THz, surpassing most of its counterparts. By leveraging in-sensor computing, our device effectively suppresses noise in THz detection while enhancing signal clarity through real-time edge detection and sharpening, thereby improving feature extraction and detection accuracy. By further integrating with the YOLO network, the system enables the detection and classification of objects in security screening, achieving a recall rate exceeding 90% for most of the concealed positions. These functionalities are essential for advancing the precision and reliability of THz detection in biomedical and security applications (Figure 1b,c).

2. Results and Discussion

2.1. Low-Temperature Ultrafast Synthesis of Oriented Bi_2Se_3 Films

Based on the low processing temperature, the PIS technique is compatible with heat-intolerant polymeric substrates.[15] In a typical preparation process, bismuth (Bi) and selenium (Se) thin films are alternately deposited on the flexible polyimide (PI) substrates by a thermal evaporation system, as shown in Figure 1d. Then, the thin film with alternating elemental layers is subjected to rapid high-intensity irradiation treatment at 150 °C. The temperature control system allows rapid heating rates of ≈100 K s^{-1}. It achieves a heating duration of less than one second (Figure S1, Supporting Information). This pulsed irradiation heating initiates interdiffusion across the layers, leading to the nucleation and subsequent growth of Bi_2Se_3 into a layered architecture, as illustrated in Figure 1e.

In this work, the ultrafast and low-temperature PIS synthesis process is based on a self-propagating combustion mechanism.[15,16] The exothermic reaction of $2Bi + 3Se \rightarrow Bi_2Se_3$ is characterized by a negative formation enthalpy of ≈−140 kJ mol^{-1}, as shown in Figure 1f.[15] When a thermal pulse ignites the stacked Bi/Se layers, the exothermic reaction generates intense heat, causing a rapid local temperature rise that approaches the adiabatic limit. This creates localized high-temperature zones with self-propagating combustion characteristics, establishing optimal conditions for the interdiffusion between Bi/Se layers, nucleation, and crystal growth of Bi_2Se_3. The adiabatic temperature, calculated to be ≈722 °C, significantly surpasses the melting points of Bi (271.4 °C) and Se (220.8 °C), allowing the continuous propagation of the combustion wave.[16] Under these conditions, the generated heat is adequate to sustain the reaction until the Bi/Se reactants are fully consumed. This self-sustaining combustion mechanism facilitates rapid nucleation and eliminates the requirement for additional energy input, substantially lowering the PIS processing temperature.

To shed light on the PIS process, high-resolution transmission electron microscopic (HRTEM) images are obtained to directly reveal the heating pulse-induced transformation process. As for the alternating Bi/Se elemental layers, Figure 1g clearly displays the interfaces between Bi and Se layers, where the bright layers represent Se layers and dark layers signify Bi layers. After PIS, a well-crystallized Bi_2Se_3 thin film is obtained on PI substrates via a self-propagating combustion process. The HRTEM and SAED images in Figure 1h clearly show the layered structure of the Bi_2Se_3 thin films, which agree well with the rhombohedral Bi_2Se_3 structure and R $\bar{3}$ m space group.[17] The layered Bi_2Se_3 possesses a bulk band gap of ≈0.5 eV, arising from the strong spin-orbit coupling (Figure S2, Supporting Information). The grazing-incident X-ray diffraction (GIXRD) pattern in Figure 1i reveals that the Bi_2Se_3 thin film has a crystallographic c-axis aligned along the PI substrate surface normal, which takes precedence over other directions. Specifically, the diffraction peaks corresponding to out-of-plane orientations with (00l) (l = 3, 6, 9, 12, 15) peaks are pronounced after the PIS process.

Furthermore, the complete conversion process of Bi_2Se_3 films during PIS treatment was confirmed by X-ray photoelectron spectroscopy (XPS) and energy-dispersive X-ray spectroscopy (EDX) analysis (Figures S3 and S4, Supporting Information). The elemental ratio of Se and Bi was measured to be 60.1% and 39.9%, respectively, indicating the successful conversion and formation of the Bi_2Se_3 phase. The surface morphology and structural characteristics of the films were further examined using scanning electron microscopy (SEM), atomic force microscopy (AFM), and Raman mapping (Figures S5 and S6, Supporting Information). SEM images reveal a uniform and compact film structure, while AFM analysis indicates a smooth surface with a roughness (R_q) of 2.3 nm. The Raman spectra further confirm the presence of Bi_2Se_3, as evidenced by the characteristic vibrational modes.

2.2. THz Spectroscopy and Detection Performance of Bi_2Se_3 Sensors

To investigate the THz conversion efficiency of Bi_2Se_3 thin films on PI substrate, their THz absorbance property is investigated by THz time-domain spectroscopy (TDS). As shown in **Figures** 2a-c and S7 (Supporting Information), the Bi_2Se_3/PI samples demonstrate obvious absorption in low-frequency THz regions up to 2 THz, highlighting their potential in THz detection. Note that the Bi_2Se_3 material has an absorption coefficient of 2.98 × 10^6 cm^{-1},[18] better than most typical thermoelectric materials (Figure 2d), by which good THz-thermal conversion efficiency would be expected on Bi_2Se_3. After the THz-sensitive Bi_2Se_3 thin films were fabricated on PI substrates, paired Ni electrodes were evaporated on the patterned thin film to form a metal-Bi_2Se_3-metal THz detector (Figure 2e). Since the work function of the Bi_2Se_3 sample is ≈5.3 eV, a metal contact of Ni (with a work function of 5.1 eV) is used in this work. As a result, ohmic-like contacts between Bi_2Se_3 and Ni are realized, as witnessed by the linear relationship in the *I*–*V* curve (Figure 2f).

After that, a THz source (IMPATT diode) with a frequency of 0.3 THz was used to check the THz detection performance of Bi_2Se_3 films on PI substrates. Complete details regarding the experimental setup and dimensional parameters of the device are provided in Figures S8 and S9 (Supporting Information). The frequency bands from 0.275 to 0.45 THz have minimal attenuation induced by environmental water absorption.[19] This allows for long-distance high-capacity transmission with minimal signal degradation. The voltage responsivity (*R*) is calculated to be 200 V W^{-1} by using the relation $R = V_{ph}/(P_{THz} \times S_\lambda)$, where S_λ is determined to be $\lambda^2/4$ and P_{THz} is the incident THz intensity.[20] Figure 2g,h exhibits the fast optical response in a switching measurement with 0.3 THz irradiation, and the reproducible response under cycling switches in Figure S10 (Supporting Information) indicates good THz detection stability. At a chopping frequency of 1 Hz, the response times, determined by the duration required for the photocurrent to rise from 10% to 90% of its maximum value, are measured to be ≈5 ms (Figure 2i; Figure S11, Supporting Information). Subsequently, the noise-equivalent power (NEP) of our Bi_2Se_3/PI devices can reach less than 30 $pW/Hz^{0.5}$ without external bias at ambient temperature (see the details in Experimental Section). A comparison of THz detector performance made from different topological materials and other low-dimensional materials is provided in Table S1, which shows the good performance of our devices in terms of NEP, responsivity, flexibility, and scalability.

The PTE response behavior is distinguished from other THz detection mechanisms, such as bolometric response and plasma wave (PW) photoexcitation.[5,21] 1) Note that the bolometer is based on the photothermal-induced conductivity variation in thermosensitive materials. An essential criterion for the bolometers is that an external bias needs to be applied to the device; otherwise, no photocurrent will be generated. For our device, when $V = 0$ V, the output signal is still generated by THz excitation (Figure 2g), which excludes the possibility of a bolometric effect.[5] 2) Besides the thermal-driven effects, PW photoexcitation would also output V_{ph} and photocurrent signals due to the capacitive-coupling-induced Dyakonov-Shur rectification.[21] The PW photoresponse is expected to increase with the applied bias because of the forced injection of electrons in the channel and the enhanced asymmetry induced by the current. Accordingly, the lack of photocurrent (defined as $I_{light} - I_{dark}$) dependence on *V* indicates that the PW effect is negligible. 3) In contrast, the Seebeck effect, characterized by a temperature gradient induced

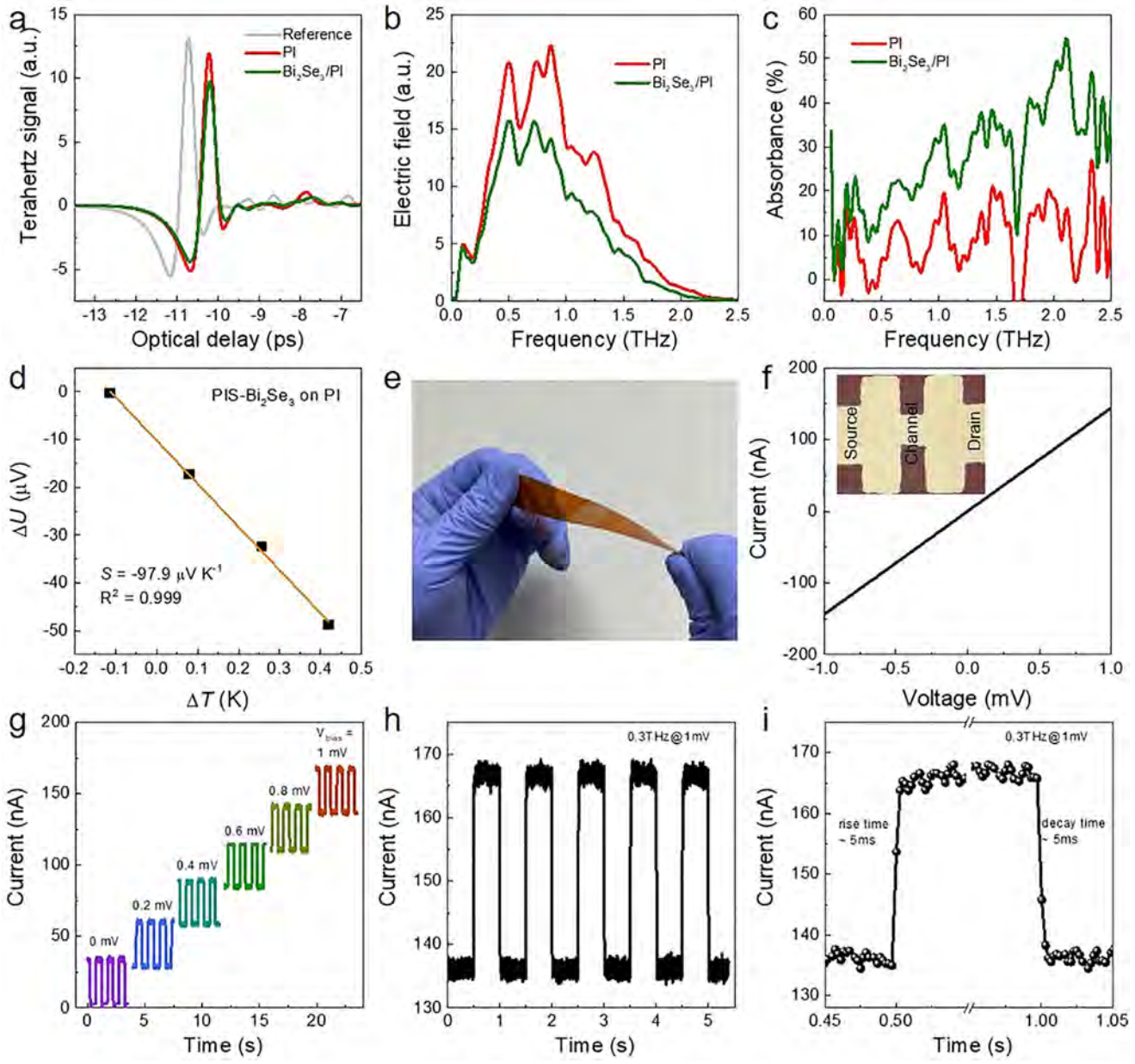

Figure 2. a) THz time-domain, b) frequency-domain, and c) absorbance spectroscopy of the PI substrate and the Bi_2Se_3 film/PI substrate. d) Summary of the thermal conductivity and absorption coefficient of typical thermoelectric materials. e) Photograph of Bi_2Se_3 THz detector on the flexible PI substrate. f) *I–V* curve of the Bi_2Se_3 device with Ni contact. The inset shows the optical image. g) Output current of switching Bi_2Se_3/PI devices as a function of bias measured in voltage mode. h) Output current of Bi_2Se_3/PI devices under 1 mV bias, and i) the corresponding response of a single switching cycle.

by nonuniform irradiation and, thus, a corresponding electric potential difference, can be identified as the THz detection mechanism of PTE devices in this work.

2.3. PTE Conversion and Bi-Directional Response of Bi_2Se_3/PI Devices

The PTE effect includes two successive processes (i.e., photothermal conversion and Seebeck effect), enabling the THz signals to be efficiently transferred into electrical readouts (**Figure** 3a,b).[22–24] 1) Generally, the thermal conductivity of the sample significantly influences the temperature distribution in the photothermal conversion process. The material absorbs photons to generate non-equilibrium charge carriers, dissipating energy via electron-phonon scattering, leading to localized lattice heating.[25] The Bi_2Se_3 material has a thermal conductivity down to 0.55 $W\ m^{-1}K^{-1}$,[26] lower than most typical thermoelectric materials (Table S2, Supporting Information), meaning a larger temperature gradient can be formed on Bi_2Se_3. Besides, based on a substrate thermal coupling effect, since polymeric PI substrates have a low thermal diffusivity coefficient of 0.21 $mm^2\ s^{-1}$, an

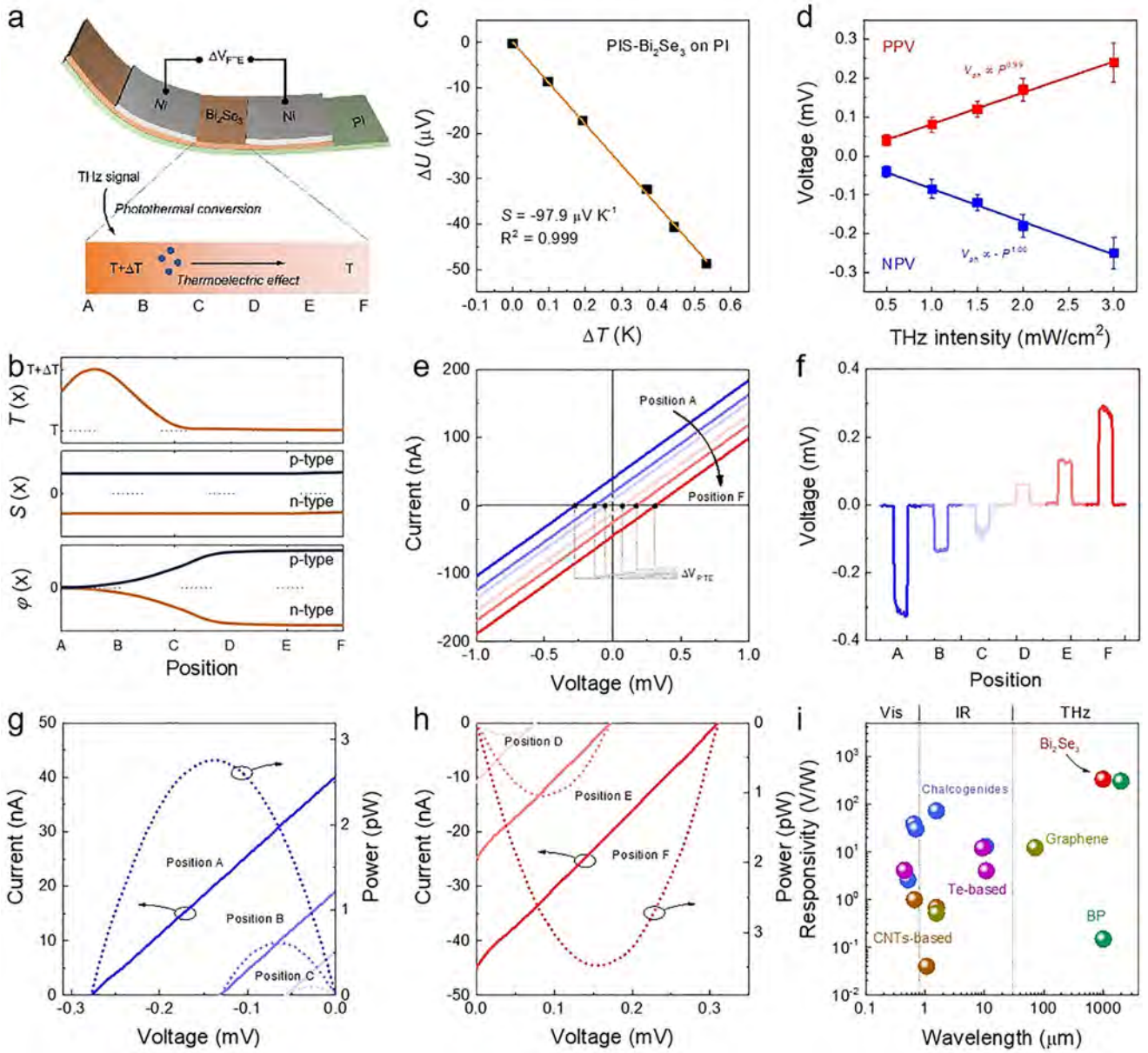

Figure 3. a) Illustration of the PTE conversion processes in Bi_2Se_3/PI devices. b) Temperature, Seebeck coefficient, and electric potential differences in the Bi_2Se_3 channel. c) Room-temperature Seebeck effect and coefficient of Bi_2Se_3 films. d) Linear relationship between THz intensity and photovoltage measured in current mode. e) *I*–*V* curve of Bi_2Se_3/PI devices measured at 0.3 THz with different illuminated positions. f) Photovoltage of Bi_2Se_3/PI devices with different illuminated positions measured in current mode. g,h) Output current (solid line) as a function of applied voltage with different THz illuminated positions. The output power (dotted line) is calculated by multiplying the current and the corresponding voltage. i) Summary of the responsivity of PTE photodetectors.

enhanced localized temperature distribution would also be expected on the Bi_2Se_3/PI structure.[15] 2) After the photothermal conversion process, the thermoelectric effect continues to play a key role in PTE THz detection. A symmetric heat dissipation creates a measurable $\Delta T/\Delta x$, inducing the PTE voltage via the Seebeck effect ($V_{PTE} = -S\Delta T$).[27] In this work, the Seebeck coefficient of Bi_2Se_3 is measured to be negative as $-97.9\ \mu V\ K^{-1}$, indicating its n-type behavior and major carriers of electrons (Figure 3c).[15] Such Seebeck coefficient is comparable with other Bi_2Se_3 films fabricated by conventional methods (Table S3, Supporting Information), but with lower fabrication temperature and faster deposition process. Overall, the enhanced temperature distribution and Seebeck coefficient obtained in the Bi_2Se_3/PI structure promise to realize high-sensitivity PTE-type THz detection.

When the nonuniform THz signal irradiates Bi_2Se_3 PTE devices, a temperature gradient is generated along the channel, driving the major carriers (i.e., electrons of Bi_2Se_3) to move from warm to cold sides.[22,23,28] As shown in Figure 3d, the ideal linear

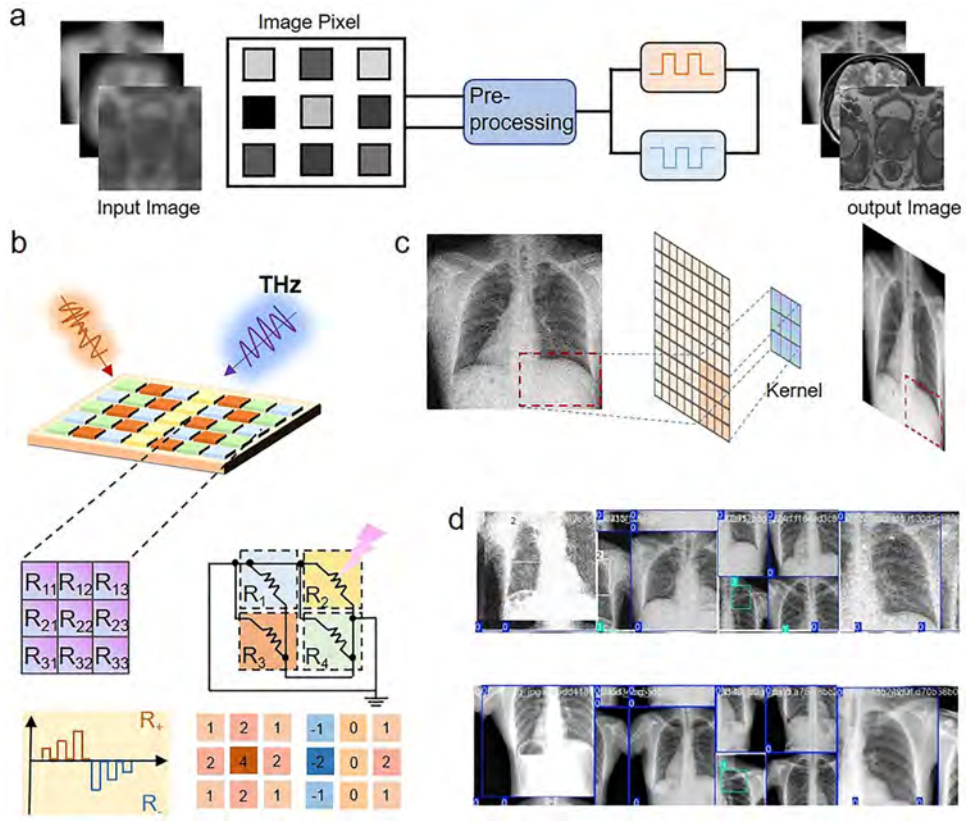

Figure 4. a) Blurred medical images undergo preprocessing to enhance clarity and improve diagnostic accuracy. b) Schematic illustration of the simultaneous sensing and response process, wherein the PTE array functions as a convolutional kernel to facilitate real-time noise suppression and feature enhancement. c) A chest image severely degraded by Gaussian noise is reconstructed into a high-clarity image through the convolution operation. d) Lesion feature detection before and after noise filtering, demonstrating the integration of the PTE array for improved medical image analysis and diagnostic precision. The chest images were obtained from the tbx-11k dataset.[39]

relationship between THz intensity and output voltage, indicated by a fitting factor close to 1, rules out the photoconductive and bolometric effects in this work.[15,28] Unlike photoconductive detectors, the PTE voltage could be modulated or even reversed by manipulating the THz illumination position. Specifically, an opposite maximum photovoltage (V_{PTE}) of ±300 μV and photocurrent ($I_{PTE} = \sigma V_{PTE}$) of ±35 nA were obtained at two ends of the Bi_2Se_3 channel (Figure 3e). At the same time, a zero V_{PTE} is obtained at the channel center position (Figure 3f). These results agree well with the typical PTE mechanism.[29,30] The ΔT can be calculated using the device output voltage and the Seebeck coefficient of the Bi_2Se_3 material. In this case, the maximum ΔT is estimated to be ≈3 K, induced by the THz photothermal conversion process on Bi_2Se_3/PI.

The bi-directional positive/negative PTE responses with well-symmetric characteristics were obtained while the THz signal illuminates two opposite channel positions. Through position-sensitive modulation, the THz detector achieves versatile responses, including positive photovoltage (PPV), negative photovoltage (NPV), and zero photovoltage (ZPV) under illumination. This behavior parallels the signal acquisition process in sensory cells. It emulates the "excitation" and "inhibition" mechanisms, resembling the fundamental functions of synaptic activity.[31,32] The output power as a function of the THz-illuminated position is also plotted in the Figure 3g,h, with the highest output electric power reaching above 3 pW when THz is illuminated at the ends of the channel. Overall, the obtained PTE THz detection performance metrics, including responsivity and response time, are comparable to those of THz detectors using state-of-the-art materials (Figure 3i; Table S4, Supporting Information).

2.4. Noise Filtering and Feature Enhancement in Medical Imaging

Medical imaging is an essential tool in clinical diagnostics, yet it is frequently compromised by noise contamination, which obscures critical features and reduces diagnostic accuracy. Conventional noise filtering techniques rely on software-based post-processing, which demands significant computational resources and increases processing latency, making real-time applications challenging. To address this issue, in-sensor computing has emerged as an innovative approach, directly integrating preprocessing capabilities within the detection hardware (**Figure 4a**).[33,34] The PTE effect in a Bi_2Se_3 array is utilized to achieve simultaneous sensing and processing, enabling real-time noise suppression and feature enhancement without external computational overhead.

The Bi_2Se_3 array not only captures incident light but also performs convolution operations through position-dependent photovoltage generation, making it an effective hardware-implemented image processing unit. By programming the illumination position, the system orchestrates PPV, NPV, and ZPV combinations, facilitating in-sensor visual feature extraction.[35] Unlike conventional imaging systems that separate detection and processing modules, the Bi_2Se_3 array merges light detection with preprocessing, achieving near-data computation. The THz-induced PTE conversion disrupts the symmetry of the electric potential along the channel, leading to a position-tunable bidirectional response that physically implements convolution. Precisely, the incident image intensity (P_j) is mapped onto the PTE array, where each pixel generates V_{ph} according to $V_{ph} = \sum R_j P_j$, with R_j representing the responsivity of each pixel (Figure 4b). The position-dependent responsivity exhibiting both positive and negative values serves as the convolutional weight of a kernel matrix, allowing direct execution of computational tasks at the sensor level.

To validate the in-sensor convolutional capability, we implemented a 3 × 3 Laplacian operator by mapping its weights onto the R_j of the array, forming a hardware convolutional kernel.[36,37] This approach enables noise filtering and edge detection, the fundamental tasks in image processing, as demonstrated in Figure 4c and Figure S12 (Supporting Information). The convolution matrix and the corresponding device responsivity mapping weights are shown in Figure S13 (Supporting Information). Furthermore, blurred and noise-degraded images were effectively reconstructed in a medical imaging scenario using the Bi_2Se_3 array. By integrating convolution in this array, lesion feature detection was significantly enhanced through noise suppression and contrast optimization (Figure 4d), highlighting the potential of Bi_2Se_3 array-enabled in-sensor computing for advanced medical diagnostics. The demonstrated system paves the way for adaptive, efficient, and high-resolution real-time medical imaging, offering a transformative solution for intelligent imaging applications.

2.5. PTE-Enhanced Terahertz Security Screening for Real-Time Concealed Object Detection

As illustrated in **Figure 5a**, THz images acquired from a security screening setup are first processed through the PTE array, where the bidirectional THz response is exploited to perform convolution operations, effectively enhancing object edges and improving image clarity. Unlike conventional imaging pipelines that require separate sensing and processing units, the PTE-enabled system merges detection and preprocessing into a single step, significantly reducing computational latency while preserving crucial object features. This in-sensor computing capability mitigates the inherent limitations of THz signals, such as low absorption efficiency and weak interaction with matter, ultimately improving target recognition. The enhanced THz images are fed into a YOLO v8-based deep learning model for automatic object detection and classification (Figure 5b; Figure S14, Supporting Information).[38] By leveraging deep learning algorithms, the system effectively compensates for signal degradation and noise, ensuring robust and accurate identification of concealed items.

The detection results (Figure 5c) demonstrate the capability of the proposed system to accurately identify and classify concealed objects with high confidence, as indicated by the precision and recall performance. To quantitatively assess detection reliability, we present precision-recall curves for ten different object categories (Figure 5d), revealing consistently high recall rates, which underscore the system's effectiveness in minimizing false negatives. Additionally, the confusion matrix (Figure 5e) provides a detailed analysis of classification accuracy, mapping true and false predictions across object categories to evaluate potential misclassification trends. The precision-recall curves of the preprocessed images demonstrated significantly improved average precision values of 93.5%, 91.2%, and 99.0% for KC, CP, and LW, respectively, compared to 85.1%, 84.6%, and 95.2% for the original images (Figure S15, Supporting Information). This enhancement highlights the effectiveness of Bi_2Se_3 array-based in-sensor computing, which leverages its excellent optoelectronic photoresponses for real-time image processing.

Furthermore, this strategy extends to noise-filtered chest lesion detection, demonstrating its broader applicability in medical diagnostics and security screening. Figure S16 (Supporting Information) compares the precision-recall curves before and after noise filtering with the corresponding average precision values summarized in Figure S17 (Supporting Information). Integrating Bi_2Se_3 array-based in-sensor computing with AI-driven classification enhances detection accuracy while minimizing external computational overhead. Combining THz detection, in-sensor preprocessing, and neural network-based classification enables real-time, high-fidelity object recognition for different applications, such as airport security, border control, and concealed weapon detection. The synergy between advanced optoelectronic materials and AI-driven processing offers a scalable and energy-efficient alternative to conventional THz detection, paving the way for next-generation intelligent security screening systems.

3. Conclusion

This work demonstrates a Bi_2Se_3-based THz detection array with a tunable thermally coupled bi-directional response, synthesized via low-temperature PIS. The device enables adaptive in-sensor computing, leveraging the intrinsic PTE effect, achieving real-time noise suppression, edge detection, and feature extraction. Operating in a self-powered mode, it delivers a responsivity of 200 V W^{-1} and a response time below 5 ms at 0.3 THz. Furthermore, integration with the YOLO neural network enables high-precision concealed object classification in processed images, achieving over 90% recall rate. These findings establish a transformative framework for intelligent THz sensing, offering a scalable pathway toward high-efficiency biomedical diagnostics and security screening.

4. Experimental Section

Material Synthesis: The PIS technique was compatible with various polymeric substrates (e.g., PI, PET, and PDMS). In a typical preparation process, Bi and Se layers were alternately deposited on the flexible substrate by a thermal evaporation system under a high vacuum (10^{-7} Torr). The thickness of the elemental layer was monitored by the quartz crystal installed in the evaporation chamber, and the evaporation rate was ≈1 Å s^{-1}.

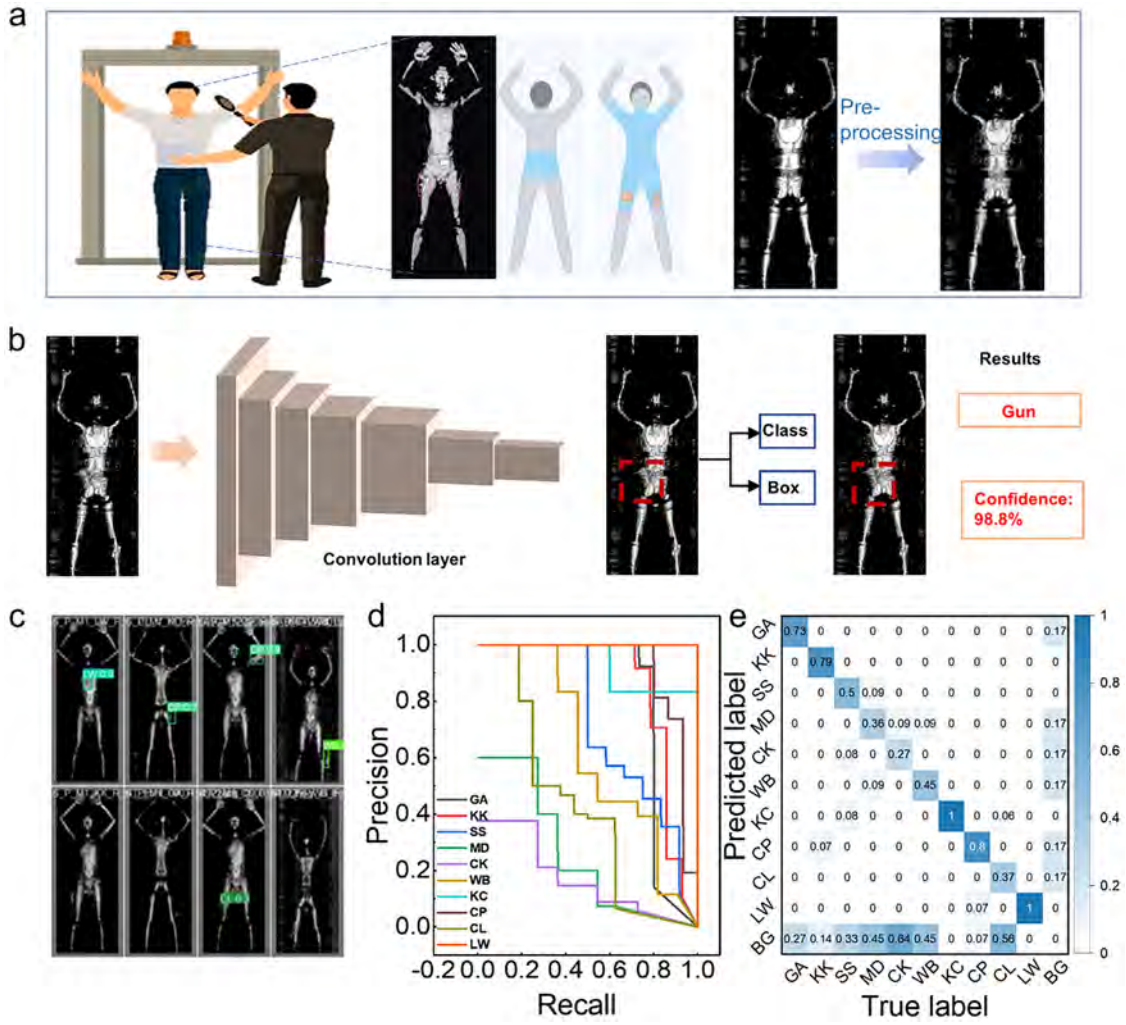

Figure 5. a) Schematic illustration of a THz security detection system for identifying concealed objects carried by the human body. The acquired detection images undergo convolutional processing via the PTE array to enhance edge clarity. b) Processed images are integrated with the YOLO v8 network for object detection and classification. The terahertz detection images were sourced from the Active Terahertz Imaging Datasets. c) Visualization of the target detection results, highlighting successfully identified objects. d) Recall-precision curves for ten different concealed object categories, demonstrating the detection performance. e) Confusion matrix illustrating the classification accuracy and misclassification distribution among different object categories.

A shadow mask was used to pattern the channel to ensure accurate data extraction. Then, the thin film with alternating elemental layers was subjected to rapid radiation treatment to form Bi_2Se_3. In this setup, the high-intensity radiation emitted by the tungsten halogen lamp rapidly heats the sample to a predetermined temperature within seconds. The temperature control system, designed for precision, achieves a rapid heating rate of $\approx$100 K s^{-1} and a heating duration of less than 1 second. Simultaneously, a continuous flow of inert argon gas was employed to shield the film from potential oxidation.

Material Characterization: The crystal structures of Bi_2Se_3 thin films were initially analyzed by X-ray diffraction via a Rigaku SmartLab X-ray Diffractometer. Raman spectra and mapping were generated by a WITec alpha300 R Raman System. To measure the compositions and chemical states of the materials, an X-ray photoelectron spectrometer was used based on a Thermo ESCALAB 250Xi system. The AFM was performed using Bruker 'MultiMode 8' Atomic Force Microscope System. The SEM of the Bi_2Se_3 film was performed using JSM-IT500, JEOL. The EDX spectrum was collected by the energy-dispersive X-ray fluorescence spectrometer of SHIMADZU (EDX-7200). The crystal structure was checked by a high-resolution transmission electron microscope (2100F, JEOL). The Seebeck coefficient was determined by a thermoelectric testing system (CTA-3, Cryoall).

Device Fabrication and Characterization: After Bi_2Se_3 thin film fabrication on PI substrates, 50-nm-thick Ni electrodes were deposited with a thermal evaporation rate of 2 Å s^{-1}. A semiconductor analyzer (Agilent 4155C) was employed to measure the electrical properties of Bi_2Se_3 films in a dark environment. The 0.3-THz continuous wave was generated by an impact ionization avalanche transit time diode (IMPATT diode, TeraSense) with a maximum output power of $\approx$10 mW, and an arbitrary function generator (AFG 2005) was employed to control the switching operation of the THz source through TTL trigger modulation. Then, the modulated THz was reflected and focused by a pair of parabolic mirrors onto the PTE device. The power of the THz radiation was calibrated using a power meter (THZ-20, SLT). The diffraction-limited area (S_λ) of incident THz radiation was determined to be the effective area, of which the THz intensity has a two-dimensional Gaussian distribution. After that, a precise moving platform was used to control the THz illumination position. Noise-equivalent power (NEP) was given by $NEP = \nu_n/R$, where ν_n and R represent the root

mean square of the noise voltage and voltage responsivity, respectively. Furthermore, $\nu_n = (\nu_t^2 + \nu_s^2)^{1/2} = (4k_BTr + 2eI_dr^2)^{1/2}$, ν_t and V_s represent the thermal Johnson–Nyquist and shot noise, respectively; k_B is the Boltzmann constant, T is the ambient temperature, e is the elementary charge, and I_d is the bias current.[9] The voltage responsivity (R) is calculated by using the relation $R = V_{ph}/(P_{THz} \times S_\lambda)$, where S_λ is determined to be $\lambda^2/4$ and P_{THz} is the incident THz intensity.[20]

Datasets and Usage Description: In this study, chest X-ray images were obtained from the TBX11K dataset, which provides a diverse collection of thoracic radiographs.[39] The dataset was publicly available at the following link: https://datasetninja.com/tbx-11k. The terahertz detection images were sourced from the Active Terahertz Imaging Datasets, which offer a range of terahertz imaging samples for various detection and analysis tasks. This dataset can be accessed at: https://linglix.github.io/THz_Dataset/#dataset. Both datasets were used to analyze imaging characteristics under different conditions. Preprocessing and data augmentation were performed using Python and MATLAB to ensure consistency and compatibility with the proposed framework.

Convolutional Image Processing: Grayscale images were initially generated using custom scripts to simulate the required datasets for testing. The images were designed to reflect various real-world patterns and scenarios relevant to the study. The images were subjected to convolutional operations, where the high-symmetry bi-directional THz response characteristics of the photodetector array were utilized as convolutional kernels. The convolutional filters mapped the light responsivity characteristics onto the image, extracting key features such as edges, textures, and spatial patterns. All operations, including image manipulation and convolutional processing, were automated and controlled through Python scripts, ensuring reproducibility and consistency.

Supporting Information

Supporting Information is available from the Wiley Online Library or from the author.

Acknowledgements

H.S. and Y.Z. contributed equally to this work. This work was supported by a fellowship award from the Research Grants Council of the Hong Kong Special Administrative Region, China (CityURFS2021-1S04), the Science and Technology Innovation Commission of Shenzhen Municipality (Project No. JCYJ20230807114910021), Guangdong Basic and Applied Basic Research Fund (Project No. 2024A1515011922), and supported by the "111 Center" (Project No. B25033).

Conflict of Interest

The authors declare no conflict of interest.

Data Availability Statement

The data that support the findings of this study are available from the corresponding author upon reasonable request.

Keywords

flexible device, in-sensor computing, photothermoelectric, terahertz detection

Received: March 25, 2025
Revised: July 2, 2025
Published online:

[1] X. Li, D. Mengu, N. T. Yardimci, D. Turan, A. Charkhesht, A. Ozcan, M. Jarrahi, *Nat. Photonics* **2024**, *18*, 139.
[2] G. B. Wu, J. Chen, C. Yang, K. F. Chan, M. K. Chen, D. P. Tsai, C. H. Chan, *Proc. IEEE* **2024**, *112*, 1033.
[3] C. W. Berry, N. Wang, M. R. Hashemi, M. Unlu, M. Jarrahi, *Nat. Commun.* **2013**, *4*, 1622.
[4] X. Li, J. Li, Y. Li, A. Ozcan, M. Jarrahi, *Light* **2023**, *12*, 233.
[5] Q. Qiu, Z. Huang, *Adv. Mater.* **2021**, *33*, 2008126.
[6] J. Zhang, Z. Hu, Q. Yang, S. Sun, F. Liu, H. Xu, X. Wang, Y. Zhao, N. Zhou, G. Dong, H. Zhang, R. Yang, L. Wang, W. Hu, *Adv. Mater.* **2025**, *37*, 2410275.
[7] Z. Hu, L. Zhang, A. Chakraborty, G. D'Olimpio, J. Fujii, A. Ge, Y. Zhou, C. Liu, A. Agarwal, I. Vobornik, D. Farias, C.-N. Kuo, C. S. Lue, A. Politano, S.-W. Wang, W. Hu, X. Chen, W. Lu, L., *Adv. Mater.* **2023**, *35*, 2209557.
[8] L. Wang, L. Han, W. Guo, L. Zhang, C. Yao, Z. Chen, Y. Chen, C. Guo, K. Zhang, C.-N. Kuo, C. S. Lue, A. Politano, H. Xing, M. Jiang, X. Yu, X. Chen, W. Lu, *Light: Sci. Appl.* **2022**, *11*, 53.
[9] D. Wang, L. Yang, Z. Hu, F. Wang, Y. Yang, X. Pan, Z. Dong, S. Tian, L. Zhang, L. Han, M. Jiang, K. Tang, F. Dai, K. Zhang, W. Lu, X. Chen, L. Wang, W. Hu, *Nat. Commun.* **2025**, *16*, 25.
[10] Z. Jin, J. Lou, F. Shu, Z. Hong, C.-W. Qiu, *Research* **2025**, *8*, 0562.
[11] N. Wang, S. Cakmakyapan, Y.-J. Lin, H. Javadi, M. Jarrahi, *Nat. Astron.* **2019**, *3*, 977.
[12] G.-B. Wu, J. Y. Dai, Q. Cheng, T. J. Cui, C. H. Chan, *Nat. Electron.* **2022**, *5*, 808.
[13] L. Xu, J. Liu, X. Guo, S. Liu, X. Lai, J. Wang, M. Yu, Z. Xie, H. Peng, X. Zou, X. Wang, R. Huang, M. He, *Nat. Commun.* **2024**, *15*, 9011.
[14] Y. Yang, C. Pan, Y. Li, X. Yangdong, P. Wang, Z.-A. Li, S. Wang, W. Yu, G. Liu, B. Cheng, Z. Di, S.-J. Liang, F. Miao, *Nat. Electron.* **2024**, *7*, 225.
[15] Y. Zhang, Y. Meng, L. Wang, C. Lan, Q. Quan, W. Wang, Z. Lai, W. Wang, Y. Li, D. Yin, D. Li, P. Xie, D. Chen, Z. Yang, S. Yip, Y. Lu, C.-Y. Wong, J. C. Ho, *Nat. Commun.* **2024**, *15*, 728.
[16] X. Su, F. Fu, Y. Yan, G. Zheng, T. Liang, Q. Zhang, X. Cheng, D. Yang, H. Chi, X. Tang, Q. Zhang, C. Uher, *Nat. Commun.* **2014**, *5*, 4908.
[17] J. Zhang, Z. Peng, A. Soni, Y. Zhao, Y. Xiong, B. Peng, J. Wang, M. S. Dresselhaus, Q. Xiong, *Nano Lett.* **2011**, *11*, 2407.
[18] T. Manjulavalli, T. Balasubramanian, D. Nataraj, *Chalcogenide Lett.* **2008**, *5*, 297.
[19] M. J. Marcus, *IEEE Wireless Commun* **2016**, *23*, 2.
[20] L. Zhang, Z. Dong, L. Wang, Y. Hu, C. Guo, L. Guo, Y. Chen, L. Han, K. Zhang, S. Tian, C. Yao, Z. Chen, M. Cai, M. Jiang, H. Xing, X. Yu, X. Chen, K. Zhang, W. Lu, *Adv. Sci. (Weinh)* **2021**, *8*, 2102088.
[21] M. Mittendorff, S. Winnerl, T. E. Murphy, *Adv. Opt. Mater.* **2021**, *9*, 2001500.
[22] M. Dai, X. Zhang, Q. J. Wang, *Adv. Funct. Mater.* **2024**, *34*, 2312872.
[23] X. Cai, A. B. Sushkov, R. J. Suess, M. M. Jadidi, G. S. Jenkins, L. O. Nyakiti, R. L. Myers-Ward, S. Li, J. Yan, D. K. Gaskill, T. E. Murphy, H. D. Drew, M. S. Fuhrer, *Nat. Nanotechnol.* **2014**, *9*, 814.
[24] C. Guo, Y. Hu, G. Chen, D. Wei, L. Zhang, Z. Chen, W. Guo, H. Xu, C.-N. Kuo, C. S. Lue, X. Bo, X. Wan, L. Wang, A. Politano, X. Chen, W. Lu, *Sci. Adv.* *6*, abb6500.
[25] X. Lu, L. Sun, P. Jiang, X. Bao, *Adv. Mater.* **2019**, *31*, 1902044.
[26] Y. Min, J. W. Roh, H. Yang, M. Park, S. I. Kim, S. Hwang, S. M. Lee, K. H. Lee, U. Jeong, *Adv. Mater.* **2013**, *25*, 1425.
[27] P. Sun, B. Wei, J. Zhang, J. M. Tomczak, A. Strydom, M. Søndergaard, B. B. Iversen, F. Steglich, *Nat. Commun.* **2015**, *6*, 7475.
[28] M. Dai, C. Wang, M. Ye, S. Zhu, S. Han, F. Sun, W. Chen, Y. Jin, Y. Chua, Q. J. Wang, *ACS Nano* **2022**, *16*, 295.
[29] F. Wang, S. Zhu, W. Chen, J. Han, R. Duan, C. Wang, M. Dai, F. Sun, Y. Jin, Q. J. Wang, *Nat. Nanotechnol.* **2024**, *19*, 455.
[30] M. Dai, C. Wang, B. Qiang, Y. Jin, M. Ye, F. Wang, F. Sun, X. Zhang, Y. Luo, Q. J. Wang, *Nat. Commun.* **2023**, *14*, 3421.

[31] J. Fu, C. Nie, F. Sun, G. Li, H. Shi, X. Wei, *Sci. Adv.* **2024**, *10*, adk8199.
[32] L. Pi, P. Wang, S.-J. Liang, P. Luo, H. Wang, D. Li, Z. Li, P. Chen, X. Zhou, F. Miao, T. Zhai, *Nat. Electron.* **2022**, *5*, 248.
[33] B. Ouyang, J. Wang, G. Zeng, J. Yan, Y. Zhou, X. Jiang, B. Shao, Y. Chai, *Nat. Electron.* **2024**, *7*, 705.
[34] G.-X. Zhang, Z.-C. Zhang, X.-D. Chen, L. Kang, Y. Li, F.-D. Wang, L. Shi, K. Shi, Z.-B. Liu, J.-G. Tian, T.-B. Lu, *Sci. Adv.* **2023**, *9*, adi5104.
[35] C. Jin, J. Wang, S. Yang, Y. Ding, J. Chang, W. Liu, Y. Xu, X. Shi, P. Xie, J. C. Ho, C. Wan, Z. Zheng, J. Sun, L. Liao, J. Yang, *Adv. Mater.* **2024**, *37*, 2410398.
[36] C. Han, X. Liu, X. Han, M. He, J. Han, H. Zhang, X. Hou, H. Zhou, H. Yu, Z. Wu, J. Gou, J. Wang, *Adv. Funct. Mater.* **2022**, *32*, 2209680.
[37] H. Huang, X. Liang, Y. Wang, J. Tang, Y. Li, Y. Du, W. Sun, J. Zhang, P. Yao, X. Mou, F. Xu, J. Zhang, Y. Lu, Z. Liu, J. Wang, Z. Jiang, R. Hu, Z. Wang, Q. Zhang, B. Gao, X. Bai, L. Fang, Q. Dai, H. Yin, H. Qian, H. Wu, *Nat. Nanotechnol.* **2025**, *20*, 93.
[38] D. Wan, R. Lu, B. Hu, J. Yin, S. Shen, T. Xu, X. Lang, *Adv. Eng. Inf.* **2024**, *62*, 102709.
[39] Y. Liu, Y.-H. Wu, Y. Ban, H. Wang, M.-M. Cheng, presented at *2020 IEEE/CVF Conference on Computer Vision and Pattern Recognition (CVPR)*, Seattle, WA, USA, June **2020**.